



Pulsating propagation and extinction of hydrogen detonations in ultrafine water sprays

Yong Xu, Huangwei Zhang*

Department of Mechanical Engineering, National University of Singapore, 9 Engineering Drive 1, Singapore, 117576, Singapore

ARTICLE INFO

Article history:

Received 16 October 2021

Revised 26 February 2022

Accepted 26 February 2022

Keywords:

Hydrogen

Pulsating detonation

Detonation extinction

Water sprays

Mass loading

Droplet size

ABSTRACT

Pulsating detonation and extinction in stoichiometric hydrogen/oxygen/argon gas with water sprays are studied for the first time. Eulerian-Lagrangian method is employed, and the emphasis is laid on characterization of the unsteady phenomena and evolutions of chemical / flow structures in pulsating propagation and extinction. Three detonation propagation modes are found: (1) pulsating propagation, (2) propagation followed by extinction, and (3) immediate extinction. For pulsating detonation, within one cycle, the propagation speeds and the distance between reaction front (RF) and shock front (SF) change periodically. The pulsating phenomenon originates from the interactions between gas dynamics, chemical kinetics, and droplet dynamics inside the induction zone. Multiple pressure waves are emanated from the RF within one cycle, which overtake and intensify the lead SF. An autoigniting spot arises in the shocked gas after the contact surface. The relative locations of SF, RF, shock-frame sonic point, and two-phase contact surface remain unchanged in a pulsating cycle, but their distances have periodic variations. Moreover, detonation extinction is featured by continuously increased distance between the RF and SF and quickly reduced pressure peaks, temperature, and combustion heat release. The decoupling of RF and SF leads to significantly increasing chemical timescale of the shocked mixture. The hydrodynamic structure also changes considerably when detonation extinction occurs. Moreover, the predicted map of detonation propagation and extinction illustrates that the critical mass loading for detonation extinction reduces significantly when the droplet size becomes smaller. It is also found that for the same droplet size, the average detonation speed monotonically decreases with water mass loading. However, detonation speed and pulsating frequency have a non-monotonic dependence on droplet size under a constant water mass loading.

© 2022 The Combustion Institute. Published by Elsevier Inc. All rights reserved.

1. Introduction

There are growing concerns about carbon dioxide (CO₂) emissions from fossil fuel combustion and utilization of low-carbon fuels is in high demand. Hydrogen (H₂) is deemed a clean fuel because its oxidation does not generate CO₂. However, compared to conventional hydrocarbons, H₂ is more chemically reactive, with lower ignition energy and wider flammability limit [1]. Therefore, inhibition of hydrogen ignition and explosion is of utmost importance for its practical applications. Water spray is an ideal mitigant for gas explosions [2,3], because it can absorb heat from gas phase due to large heat capacity and latent heat of evaporation [4]. Besides, the sprayed water droplets have large specific surface area and low terminal velocity, and hence can circulate in explosion area in a manner of a total flooding gas.

There have been numerous studies available about the mechanisms of water sprays in inhibiting flammable gas detonation. For instance, Thomas et al. [5] attribute detonation extinction to high heat loss due to water droplets. The water droplet diameter and loading densities are identified as key factors for detonation inhibition. Niedzielska et al. [6] also observe that small droplets have strong influence on detonation quenching due to their fast evaporation rate. Jarsalé et al. [7] find that water droplets do not alter the ratio of the hydrodynamic thickness to the cell size, but it can affect detonation stability. Besides the foregoing experimental work, Song and Zhang [8] simulate methane detonation with water mists and find that the water droplets considerably reduce the flame temperature. Recently, Watanabe et al. [9] observe that the numerical soot foils of dilute water spray detonation become more regular compared to the droplet-free detonations, and the hydrodynamic thickness is altered by the direct interactions between detonation wave and water droplets. Their results also show that droplet breakup mainly occurs near the shock front, and the average diameter of the disintegrated water droplets is independent

* Corresponding author.

E-mail address: huangwei.zhang@nus.edu.sg (H. Zhang).

on the initial propagation velocity of the shock front [10]. However, unsteady detonation behaviors caused by the added water droplets have not been focused on in these studies.

Pulsating propagation is one of the important unsteady phenomena in detonative combustion, because of the interactions between gas dynamics and chemical kinetics [11]. The wave-interaction theory by Toong and his co-workers [12,13] indicates that pulsating instability results from the periodic interactions between shock front and wave structures due to the formation of new reaction zone. This theory has been confirmed in Refs. [14–17]. Furthermore, Short et al. [18] demonstrate that the instability of regular detonation oscillations is induced by compression and expansion waves within the induction zone. For irregular oscillations, it is driven by the decoupling / coupling of reaction front and shock front. Sussman [19] find that the ratio of the heat release time to the induction time affects the longitudinal oscillation mode. Ng et al. [20,21] use bifurcation theory to analyze detonation instability and propose a stability parameter depending on the induction and reaction zone length.

Recently, Han et al. [22,23] identify four pulsating detonation modes, including mildly unstable detonation with multi- and single-period pulsations. Kim et al. [24] reveal that nonlinear temporal patterns is a function of the perturbation wavelength. This finding demonstrates that one-dimensional gaseous chaotic pulsating oscillations can be regularized by the coupling between the intrinsic instability and small perturbation. Zhao et al. [25] show that pulsating detonation of *n*-heptane/air mixtures occurs under off-stoichiometric conditions. They also observe that the pulsating frequency is considerably influenced by equivalence ratio, initial pressure, and temperature. Nonetheless, to the best of our knowledge, no studies are available hitherto about how the dispersed phase affects the pulsating detonation propagation.

In this work, Eulerian–Lagrangian method with two-way coupling is employed to predict incident detonations in ultrafine water sprays. A one-dimensional configuration filled with hydrogen/oxygen/argon mixture and ultrafine water droplets is considered, and the effects of water droplet properties on incident detonations are studied in detail. The novelties of this study include: (1) characterization of detonation pulsating propagation and extinction in gas-liquid two-phase media for the first time; (2) evolution of hydrodynamic structure in detonation pulsating propagation and failure; (3) quantification of chemical reaction information in transient detonation phenomena; and (4) prediction of a map of spray detonation behaviours considering various droplet properties. The manuscript is structured as below. The mathematical model will be clarified in Section 2, whilst the physical model will be detailed in Section 3. The results and discussion will be presented in Section 4, followed by main conclusions in Section 5. Sensitivity analysis of our numerical implementations can be found in supplementary document.

2. Mathematical model

The Eulerian–Lagrangian method is used to simulate gas–droplet two-phase reactive flows. The Eulerian equations for gas phase and Lagrangian equations for droplet phase are solved by a two-phase compressible flow solver, *RYrhoCentralFoam* [26,27], developed from OpenFOAM 6.0 [28]. The formulation and numerical method are presented below.

2.1. Gas phase

The governing equations of mass, momentum, energy, and species mass fraction are solved for gas phase. They respectively

read

$$\frac{\partial \rho}{\partial t} + \nabla \cdot [\rho \mathbf{u}] = S_{mass}, \quad (1)$$

$$\frac{\partial (\rho \mathbf{u})}{\partial t} + \nabla \cdot [\mathbf{u}(\rho \mathbf{u})] + \nabla p + \nabla \cdot \mathbf{T} = \mathbf{S}_{mom}, \quad (2)$$

$$\frac{\partial (\rho \mathbf{E})}{\partial t} + \nabla \cdot [\mathbf{u}(\rho \mathbf{E} + \mathbf{p})] + \nabla \cdot [\mathbf{T} \cdot \mathbf{u}] + \nabla \cdot \mathbf{j} = \dot{\omega}_T + S_{energy}, \quad (3)$$

$$\begin{aligned} & \frac{\partial (\rho Y_m)}{\partial t} + \nabla \cdot [\mathbf{u}(\rho Y_m)] \\ & + \nabla \cdot \mathbf{s}_m = \dot{\omega}_m + S_{species,m}, \quad (m = 1, \dots, M-1). \end{aligned} \quad (4)$$

In above equations, t is time and $\nabla \cdot (\cdot)$ is the divergence operator. ρ is the gas density, and \mathbf{u} is the gas velocity vector. p is the pressure, and T is the gas temperature. \mathbf{T} is the viscous stress tensor. In Eq. (3), \mathbf{E} is the total non-chemical energy, \mathbf{j} denotes the diffusive heat flux, and $\dot{\omega}_T$ represents the heat release rate from chemical reactions. In Eq. (4), Y_m is the mass fraction of m -th species, and M is the total species number. \mathbf{s}_m is the species mass flux, whilst $\dot{\omega}_m$ is the production or consumption rate of m -th species by all elementary reactions.

2.2. Liquid phase

The Lagrangian method is used to model the dispersed liquid phase with a large number of spherical droplets [29]. The interactions between droplets are neglected because we only study dilute water sprays with initial droplet volume fraction being generally less than 0.1% [30]. Since the ratio of gas density to the water droplet material density is well below one, the Basset force, history force, and gravity force are not considered [30]. Therefore, the governing equations of mass, momentum, and energy for a single water droplet read

$$\frac{dm_d}{dt} = -\dot{m}_d, \quad (5)$$

$$\frac{d\mathbf{u}_d}{dt} = \frac{\mathbf{F}_d + \mathbf{F}_p}{m_d}, \quad (6)$$

$$c_{p,d} \frac{dT_d}{dt} = \frac{\dot{Q}_c + \dot{Q}_{lat}}{m_d}, \quad (7)$$

where $m_d = \pi \rho_d d_d^3 / 6$ is the mass of a single droplet, and ρ_d and d_d are the droplet material density and diameter, respectively. \mathbf{u}_d is the droplet velocity vector, $c_{p,d}$ is the droplet heat capacity at constant pressure, and T_d is the droplet temperature.

The evaporation rate, \dot{m}_d , in Eq. (5) is

$$\dot{m}_d = k_c A_d W_d (c_s - c_g), \quad (8)$$

where A_d is the surface area of a single droplet, and W_d is the molecular weight of the vapor. c_s and c_g are the vapor mass concentration at the droplet surface and in the gas phase, respectively. The mass transfer coefficient, k_c , in Eq. (8) is calculated from [31]

$$Sh = \frac{k_c d_d}{D_f} = 2.0 + 0.6 Re_d^{1/2} Sc^{1/3}, \quad (9)$$

where Sh is the Sherwood number, D_f is the vapor mass diffusivity in the gas phase [32], and Sc is the Schmidt number of gas phase. The droplet Reynolds number, Re_d , is defined as

$$Re_d \equiv \frac{\rho d_d |\mathbf{u}_d - \mathbf{u}|}{\mu}. \quad (10)$$

The drag force \mathbf{F}_d in Eq. (6) is modelled as [33]

$$\mathbf{F}_d = \frac{18\mu}{\rho_d d_d^2} \frac{C_d Re_d}{24} m_d (\mathbf{u} - \mathbf{u}_d). \quad (11)$$

The drag coefficient, C_d , is estimated with [33]

$$C_d = \begin{cases} 0.424, & \text{if } Re_d \geq 1000, \\ \frac{24}{Re_d} \left(1 + \frac{1}{6} Re_d^{2/3}\right), & \text{if } Re_d < 1000. \end{cases} \quad (12)$$

Besides, the pressure gradient force \mathbf{F}_p in Eq. (6) takes the following form

$$\mathbf{F}_p = -V_d \nabla p. \quad (13)$$

Here V_d is the volume of a single water droplet.

The convective heat transfer rate \dot{Q}_c in Eq. (7) is

$$\dot{Q}_c = h_c A_d (T - T_d). \quad (14)$$

Here h_c is the convective heat transfer coefficient, following Ranz and Marshall [31]

$$Nu = h_c \frac{d_d}{k} = 2.0 + 0.6 Re_d^{1/2} Pr^{1/3}, \quad (15)$$

where Nu and Pr are the Nusselt and Prandtl numbers of gas phase, respectively. In addition, \dot{Q}_{lat} in Eq. (7) is the latent heat absorption by droplet evaporation.

The droplet effects on the gas phase are modelled with Particle-source-in-cell approach [34], which are realized with the source terms, S_{mass} , S_{mom} , S_{energy} and $S_{species,m}$, for the gas phase equations (1)–(4). They are calculated from

$$S_{mass} = \frac{1}{V_c} \sum_{i=1}^{N_d} \dot{m}_{d,i}, \quad (16)$$

$$S_{mom} = -\frac{1}{V_c} \sum_{i=1}^{N_d} (-\dot{m}_{d,i} \mathbf{u}_{d,i} + \mathbf{F}_{d,i} + \mathbf{F}_{p,i}), \quad (17)$$

$$S_{energy} = -\frac{1}{V_c} \sum_{i=1}^{N_d} (-\dot{m}_{d,i} h_v + \dot{Q}_{c,i}), \quad (18)$$

$$S_{species,m} = \begin{cases} S_{mass} \text{ for } H_2O \text{ species} \\ 0 \text{ for other species.} \end{cases} \quad (19)$$

V_c is the CFD cell volume and N_d is the droplet number in one CFD cell. The term $-\dot{m}_{d,i} \mathbf{u}_{d,i}$ is the momentum transfer due to droplet evaporation, whereas h_v is the water vapor enthalpy at the droplet temperature T_d . Hydrodynamic force work and kinetic energy carried by the vapor are not considered in Eq. (18), because they are 2–3 orders of magnitude smaller compared to other energy exchange terms for spray detonations [35].

2.3. Computational method

For the gas phase equations, second-order backward method is employed for temporal discretization and the time step is approximately $1 \sim 2e^{-11}$ s. The MUSCL-type Riemann-solver-free KNP scheme [36] with van Leer limiter is used for convective flux calculations in the momentum equations. This scheme can accurately capture the shock wave, based on the previous studies [30,37]. It is computationally efficient, since complicated manipulations (e.g., characteristic decomposition or Jacobian calculation) are avoided for flux calculations. Higher grid resolution may be needed for the KNP scheme compared to Riemann-solver-based schemes, but it is not a burden for detonation simulations since the mesh resolution is already sufficiently fine (e.g., $O(1-10 \mu\text{m})$ to resolve the detonation structure). Total variation diminishing scheme is used for the convection terms in energy and species equations. Also, second-order central differencing scheme is applied for the diffusion terms in Eqs. (2)–(4). The mechanism (13 species and 27 reactions) by Burke et al. [38] is used for predicting hydrogen detonative combustion.

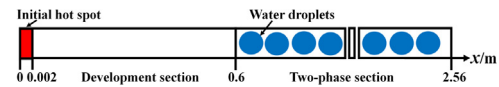


Fig. 1. Schematic of the 1D computational domain. Domain and droplet sizes not to scale.

For the liquid phase, the water droplets are tracked based on their barycentric coordinates. The equations, i.e., Eqs. (5)–(7), are integrated by first-order implicit Euler method. Meanwhile, the gas properties (e.g., velocity and temperature) at the droplet location are calculated based on linear interpolation.

The above numerical methods and the sub-models depicted in Section 2.2 have been carefully validated and verified for detonation problems in gaseous and gas–droplet two-phase flows [26,27]. They have been successfully applied for various detonation and supersonic combustion problems [25,27,39–44].

3. Physical model and numerical implementation

Incident hydrogen detonation in one-dimensional (1D) domain laden with fine water droplets are studied in this work, see Fig. 1. The 1D geometry can remove the effects of propagating transverse waves and only the longitudinal instability is retained. Besides, 1D calculations allow us to adopt fine mesh and detailed chemistry with affordable cost and hence helpful to unveil the relation between gas dynamics and chemistry in pulsating detonations. In this study, the domain is 2.56 m long (x -direction), including detonation development and gas–liquid two-phase sections. The domain is initially filled with argon diluted stoichiometric H_2/O_2 premixture (molar ratio of $H_2/O_2/Ar$: 2/1/7). The influences of gas composition on pulsating detonation have been extensively reported [15, 22, 23], and therefore would not be studied in this work.

The initial gas temperature and pressure are $T_0 = 300$ K and $p_0 = 0.2$ atm, respectively. Uniform Cartesian cells of $20 \mu\text{m}$ are used for the whole domain, and the resultant total cell number is 128,000. The Half-Reaction Length (HRL) estimated from the ZND structure of droplet-free $H_2/O_2/Ar$ detonation is $\Delta_{HRL} \approx 478 \mu\text{m}$. Considering the fact that dispersed water droplets may thicken the induction zone length due to heat and/or momentum transfer [9,35], there are at least 23 cells for Δ_{HRL} in our spray detonation simulations. Mesh resolution analysis is provided in Section A of Supplementary Document and the results confirm the sufficiency of mesh size for the gas phase.

The detonation wave is initiated by a hot spot (2000 K and 20 atm) near the left end (see Fig. 1). Changing the hot spot conditions (e.g., higher pressure) may lead to different detonation propagation behaviors at the early stage, but the two-phase section is far from the spot and therefore the initiation effects can be excluded. For the left boundary ($x=0$), the non-reflective condition is enforced for the pressure, while the zero gradient condition for other quantities [45]. Moreover, zero gradient conditions are assumed for the right boundary at $x=2.56$ m.

Monodispersed and static ($\mathbf{u}_d = 0$) water droplets are uniformly distributed in the two-phase section (i.e., $x=0.6-2.56$ m). The initial water mass loading of $z=0.01-0.5$ and droplet sizes of $d_d^0=2-15 \mu\text{m}$ will be studied in this work. Note that the mass loading is defined based on the gas properties in the two-phase section (i.e., $x > 0.6$ m). The initial temperature, material density and isobaric heat capacity of the water droplets are 300 K, 997 kg/m^3 and $4187 \text{ J/kg}\cdot\text{K}$, respectively.

The computational parcel is used in the simulations, which is an ensemble of the water droplets with the same properties (e.g., velocity, size, and temperature). Initially each cell has one parcel in the simulations and accordingly the water droplet number in each parcel, n_p , is varied based on different mass loadings. This method

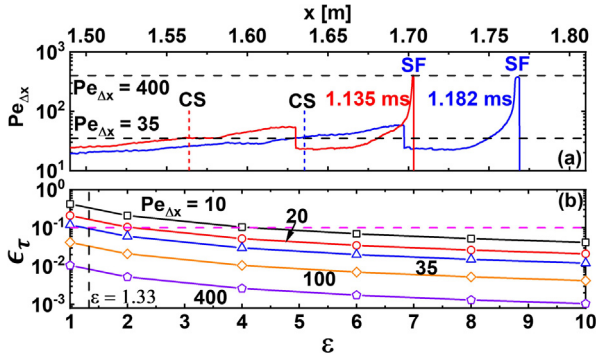


Fig. 2. (a) Spatial evolution of cell Péclet number $Pe_{\Delta x}$, and (b) evaporation timescale error ϵ_{τ} as a function of cell / droplet size ratio ϵ . CS: two-phase contact surface. SF: shock front. Results from case: $d_d^0 = 5 \mu\text{m}$ and $z = 0.07$.

is sufficient for capturing droplet evolutions and interphase coupling, based on our sensitivity analysis in Section B of Supplementary Document.

In light of the foregoing Eulerian mesh size Δ ($20 \mu\text{m}$) and initial droplet diameters d_d^0 ($2 - 15 \mu\text{m}$), their ratios, $\epsilon \equiv \Delta/d_d^0$, range from 1.33 to 10. From the tests of single droplet evaporation in stationary gas [46,47], it is shown that $\epsilon \geq 10$ is required to have accurate predictions of the droplet evaporation. Recently, Kronenburg and his co-workers [48] make relative error estimations of droplet evaporation timescale ϵ_{τ} , considering more physical and numerical factors, such as cell and droplet size ratio ϵ , initial liquid mass loading z' , cell Péclet number $Pe_{\Delta x}$, and Sherwood number Sh' . They derive the following estimations of evaporation timescale error ϵ_{τ} [48]:

$$\epsilon_{\tau} \approx \min \left[\epsilon^{-1}, z', \frac{2\pi}{3} \epsilon^{-1} \left(\frac{Pe_{\Delta x}}{Sh'} \right)^{-1} \right]. \quad (20)$$

To estimate ϵ_{τ} following Eq. (20), we calculate the cell Péclet number $Pe_{\Delta x}$ at two instants from one of our simulated cases ($d_d^0 = 5 \mu\text{m}$ and $z = 0.07$) in which detonation can stably propagate and the results are in Fig. 2. It is observed that cell Péclet number $Pe_{\Delta x}$ roughly varies from 35 to 400 within the evaporating droplet areas behind the detonation wave (between the SF and two-phase Contact Surface (CS), marked in Fig. 2a). Note that here the two-phase CS is the interface between the gas-only and gas-liquid mixtures.

Based on the results in Fig. 2(a), $2\pi\epsilon^{-1}/3 < (Pe_{\Delta x}/Sh')^{-1} < \epsilon^{-1}$ is generally valid. Figure 2(b) shows the evaporation timescale error ϵ_{τ} from the tighter conditions in Eq. (20), i.e., the last expression, considering the cell Péclet numbers of 10–400. For simplicity, $Sh' = 2$ is assumed. Apparently, inclusion of the cell Péclet number considerably reduces the requirement of ϵ to achieve an equivalent ϵ_{τ} . For example, for $Pe_{\Delta x} = 35$, to achieve $\epsilon_{\tau} < 10\%$, $\epsilon > 1.33$ (marked in Fig. 2b) is required, which is much more relaxed compared to the requirement of $\epsilon < 10$ derived from single droplet evaporation in stationary atmosphere ($Pe_{\Delta x} = 0$), which is essentially a diffusion-controlled process [46,47]. This confirms the important influences of strong convection flows (such as detonations) in modeling droplet evaporation rate. Physically, it means that the vapor released from the droplets can be swept away quickly by local convection, which considerably affects the vapor concentration difference near the droplet surface. In general, based on the above analysis, the evaporation timescale errors in our simulations ($1.33 < \epsilon < 10$) are largely less than 10%. This is also favorable for the applicability of the Eulerian–Lagrangian approach in highly resolved detonation simulations with dispersed droplets.

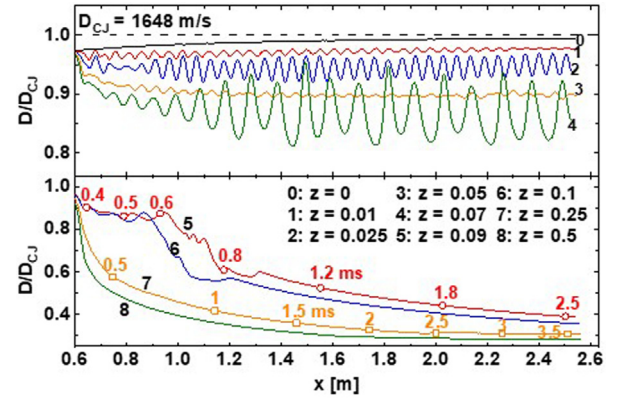


Fig. 3. Evolutions of leading shock propagation speed with various water mass loadings. $d_d^0 = 5 \mu\text{m}$. Open circles: instants studied in Figs. 10–13.

4. Results and discussion

4.1. Detonation propagation mode in water sprays

Figure 3 shows the propagation speed of the leading shock front with various water mass loadings. The initial droplet diameter is fixed to be $d_d^0 = 5 \mu\text{m}$. The results are scaled by the C–J speed, $D_{CJ} = 1648 \text{ m/s}$, of the droplet-free case ($z = 0$, or interchangeably termed as dry mixture). One can see that, after the detonation wave enters the fine water sprays ($x > 0.6 \text{ m}$), three unsteady propagation modes can be identified: (1) pulsating propagation ($z = 0.01 - 0.07$), (2) extinction after a finite propagation ($z = 0.09$ and 0.1), and (3) immediate extinction ($z = 0.25$ and 0.5). Note that the long-term fate of modes 2 and 3 may be similar in our idealized model, but it is necessary to differentiate them since immediate performance of explosion inhibition by water mists is crucial for accident prevention in real-world applications.

In the first mode (lines #1–#4 in Fig. 3), oscillating shock wave speeds are observed in the two-phase section. For instance, when $z = 0.025$, the speed varies between 1520 and 1585 m/s, whilst the pulsation frequency is approximately 28,409 Hz. The speeds in the two-phase cases are lower than that of the water-free case (line #0). In the latter, the propagation speed increases monotonically as the detonation wave propagates and is very close to the C–J speed ($D/D_{CJ} \rightarrow 1$). This indicates the significant effects of evaporating water droplets on the incident detonations. It is also seen that the magnitudes and frequencies are not monotonic with water mass loading. When $z = 0.01$ and 0.05 (lines #1 and #3), the oscillation magnitudes are much lower, compared to those with $z = 0.025$ and 0.07 . This non-monotonic change of shock speed magnitude is associated with the pressure wave strength and number, as well as the gas thermochemical properties behind the lead shock. Based on our results, as water mass loading increases, the induction zone length and chemical excitation time of the shocked gas [49] (a measure of heat release rapidity, small value typically indicates strong pressure wave) increase monotonically. Meanwhile, for low water loadings (0.01 and 0.025), single pressure wave is observed within one pulsating cycle, but there are multiple ones when the water loading is increased to 0.05 and 0.07 (see Fig. 5). For line #1 (and #3), the complex of shock front and reaction front is more stable due to stronger pressure wave(s) and shorter induction zone, compared to line #2 (and #4). The detailed analysis is provided in Section D of the Supplementary Document.

Moreover, it is observed in Fig. 3 that propagation speed decreases with increased water mass loading. For example, the mean detonation propagation speeds are 1554 and 1434 m/s for $z = 0.025$ and 0.07 , respectively. This may be because larger water mass load-

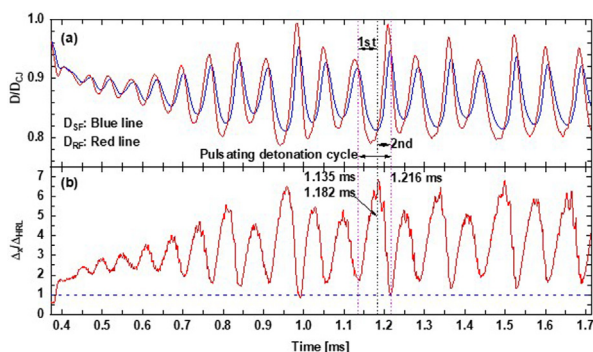


Fig. 4. Time history of (a) propagation speed of shock front D_{SF} and reaction front D_{RF} , as well as (b) the distance Δ_x between the two fronts. $d_0^* = 5 \mu\text{m}$ and $z = 0.07$.

ing has stronger weakening effect as it can absorb more energy and momentum from gas phase.

In the second mode with higher mass loading (e.g., 0.09 and 0.1, lines #5 and #6), non-monotonic changes of the shock propagation speed are present when the detonation just encroaches the two-phase section, but there are no pulsating detonations followed. After travelling a finitely long distance (about $x = 1 \text{ m}$), the shock propagation speed decays quickly, indicating the reduced interactions with the chemical reactions due to decoupling of the leading Shock Front (SF) and Reaction Front (RF). For the third mode ($z = 0.25$ and 0.5 , lines #7 and #8), decoupling of the SF and RF occurs earlier and the detonation is quenched immediately after the detonation wave arrives at the heavier water cloud, which is manifested by the monotonically decreasing shock propagation speed in the water spray area.

4.2. Pulsating detonation

Different from previous gaseous pulsating detonations [11–17], the dispersed water droplets behind the lead shock play a significant role in inducing pulsating detonation. To articulate the mechanism of pulsating detonation dynamics in the first mode, the propagation speeds of RF (D_{RF}) and SF (D_{SF}) are plotted in Fig. 4(a), which corresponds to $z = 0.07$ in Fig. 3. Note in passing that the detonation wave enters the two-phase section at 0.371 ms . After an initial transition, both RF and SF propagation speeds exhibit periodic fluctuations, but with a small phase difference. This becomes more regular since 0.7 ms . The propagation speeds of both fronts in water sprays are below than the C-J speed of the dry mixture. The pulsation behavior is accompanied by the periodic variation of the distance between the RF and SF, Δ_x , as shown in Fig. 4(b). In general, Δ_x is higher than Δ_{HRL} from the droplet-free case, which is caused by the heat absorption and/or momentum exchange of the evaporating droplets.

One pulsation cycle can be divided into the first and second stages, based on the maxima and minima of the front distance Δ_x . From Fig. 4(a), one can observe that the speeds of the RF and SF change alternately in one cycle, e.g., $1.135 \text{ ms} < t < 1.216 \text{ ms}$. At the beginning of the first cycle ($1.135 \text{ ms} < t < 1.182 \text{ ms}$), both D_{RF} and D_{SF} are high, with relatively small front distance of $\Delta_x \approx 2.0\Delta_{HRL}$. Then SF and RF decelerate, but the SF speed is still larger than the RF one. This is because the chemical reactions are significantly weakened due to the water droplets in the induction zone, which will be further discussed in Figs. 5 and 6. Accordingly, their distance Δ_x continuously increases to roughly seven times Δ_{HRL} . This indicates that the RF and SF are experiencing decoupling in this period (see 1st stage in Fig. 4). However, the pressure waves (see Fig. 5) generated by the reaction front continuously overtake the

lead shock front. Therefore, the shock travels faster than the RF, which results in an increased front distance as shown in Fig. 4(b).

Moreover, in the second half stage (i.e., $1.182 \text{ ms} < t < 1.216 \text{ ms}$), the speeds of both RF and SF increase, and the RF speed D_{RF} is always higher than the SF one D_{SF} . The faster RF is caused by the enhanced thermochemical condition of the gas between the SF and RF due to the local wave interactions (see details in Figs. 5–7). Once the hot spot is initiated after 1.203 ms , the RF speed quickly reaches the peak. At 1.216 ms , their distance is close to the HRL of dry mixture Δ_{HRL} . Nonetheless, such coupling is almost instantaneous, and the RF and SF start the next pulsation cycle with gradually increased Δ_x , which leads to a galloping movement when the detonation wave propagates in the water spray cloud.

Figure 5 shows the evolutions of the gas pressure, temperature, and Heat Release Rate (HRR) within the pulsation cycle discussed above. For the first stage of the cycle in Fig. 5(a)–(c), the decoupling of the SF and RF is characterized by gradual reduction of shock pressure, gas temperature, and maximum HRR. A key phenomenon observed from Fig. 5(a) is that multiple pressure waves, e.g., labelled with P_1 and P_2 , are generated due to the strong heat release from the RF. Combustion-induced pressure pulse is also observed during a detonation failure / re-initiation process by Tang-Yuk et al. [50]. Due to the evaporating water droplets, the thermodynamic conditions in the induction zone are significantly affected by energy absorption and/or momentum extraction. They lead to longer induction zone and lower chemical reactivity of the gas therein. Therefore, multiple pressure waves can occur and surge forward, thereby continuously modulating the gas thermochemical conditions. These new pressure waves ultimately overtake the lead SF, thereby continuously enhancing the leading shock intensity, as seen from the last several profiles of the 1st stage from Fig. 5(a). The wave interactions between the RF and SF are also reported in previous studies on gaseous galloping detonations [12,15,17,18,25]. In the 2nd stage in Fig. 5(c)–(d), this phenomenon repeatedly occurs, and the leading shock pressure increases quickly from 1.182 ms to 1.203 ms . The mutual enhancement between the RF and pressure wave becomes strong after 1.2 ms , featured by increased peak pressure and HRR. Unlike the pulsation mechanism discussed, e.g., by Yungster and Radhakrishnan for H_2/air detonations [15], single pressure wave is not sufficient to enhance the shocked gas reactivity above the autoignition threshold to induce localized hot spot and deflagration-to-detonation transition.

The detailed evolutions between 1.203 and 1.209 ms are presented in Fig. 6. A pressure wave emanated from the RF is clearly observed at 1.203 ms , which penetrates the leading SF at 1.206 ms and the shock pressure is hence increased by 22.4% compared to 1.203 ms . Meanwhile, a rarefaction wave and downstream facing contact surface are generated, and the latter demarcates the relatively hot and cold shocked gas. At 1.207 ms , one autoigniting spot (marked as AS) arises near the contact surface and at the foot of the RF, which corresponds to increased HRR, temperature, and consumption of the local hydrogen. This location is more favourable for autoignition, because of higher temperature behind the contact surface [51] and radical diffusion from the RF. Double HRR peaks appear behind the leading SF: the left peak is from the original detonative combustion, whilst the right is induced by combustion of the shocked $\text{H}_2/\text{O}_2/\text{Ar}$ mixture.

At 1.2078 ms , left- and right-running (in the shock frame) autoigniting fronts (AFL/AFR) evolve from the AS, resulting in three heat release peaks. The AFL consumes the mixture ahead of RF and collides with the RF, leading to reduced heat release. The original RF ultimately fades, and the AFR induced by the reactive spot gradually becomes strong and propagates towards the leading SF at 1.209 ms . Therefore, this leads to a relay between the two RFs in one pulsation cycle. The distance between the new RF and SF approaches Δ_{HRL} at the end of the pulsating detonation cycle, as

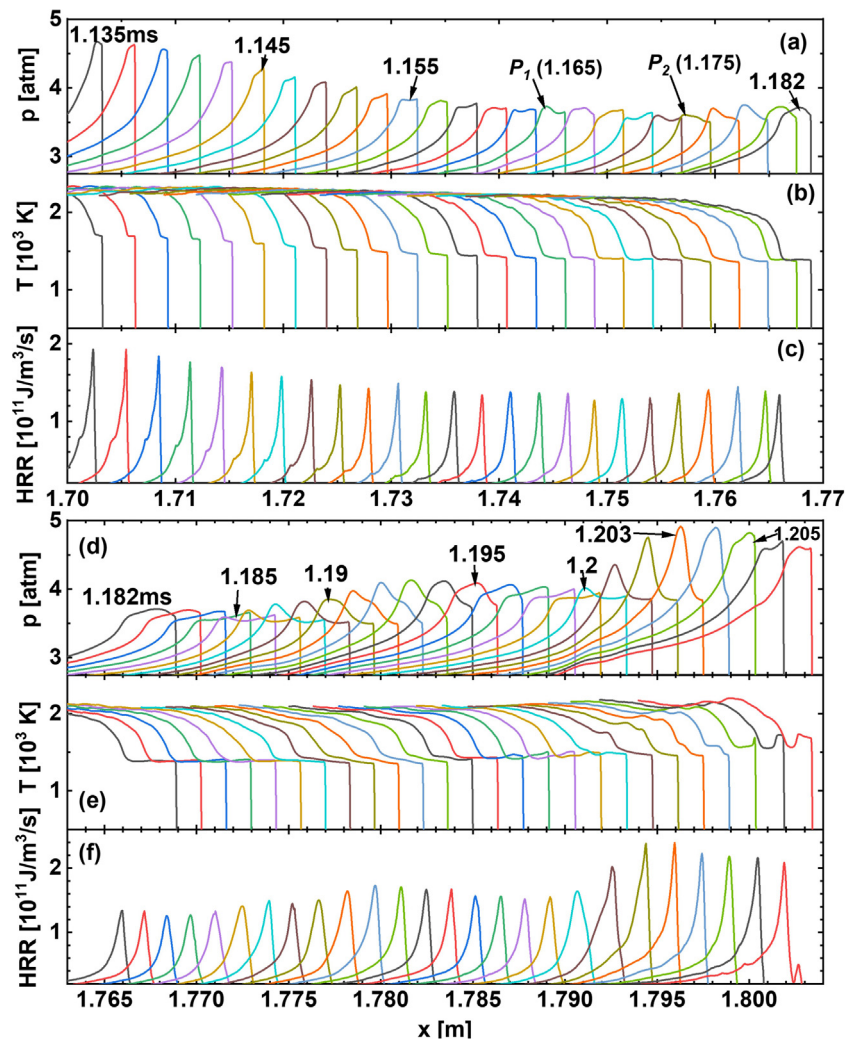


Fig. 5. Profiles of (a, d) pressure, (b, e) temperature, and (c, f) heat release rate within one pulsating detonation cycle marked in Fig. 4. The 1st stage: (a)–(c); 2nd stage: (d)–(f). $d_p^0 = 5 \mu\text{m}$ and $z = 0.07$.

shown in Fig. 4(b). However, at this instant, the RF speed is lower than that of the SF, and therefore their distance would increase again, to initiate an ensuing cycle.

The evolutions of the thermochemical structure in Fig. 6 are further quantified through chemical explosive mode analysis [52–56]. Detailed information about this method can be found in Refs. [52,56–58] Figure 7. shows the spatial evolutions of eigen values of the chemical Jacobian and explosion indices (EI) for temperature and key radicals between the RF and SF at four instants. The EI is calculated based on the eigenvectors associated with the chemical explosive mode [58–60], i.e., $\text{EI} = |\mathbf{a}_e \otimes \mathbf{b}_e^T| / \sum |\mathbf{a}_e \otimes \mathbf{b}_e^T|$, where “ \otimes ” denotes element-wise multiplication of two vectors. Larger radical EI suggests higher significance of the chemical runaway (chain-branching reactions) in local chemical reaction, whilst thermal runaway proceeds if the gas temperature plays a more important role [52]. Gas temperature profiles are also presented for reference, which are colored by logarithmic expression of the eigen value of chemical Jacobian λ_e , i.e., $\lambda_{CEM} \equiv \text{sign}[\text{Re}(\lambda_e)] \cdot \log_{10}[1 + |\text{Re}(\lambda_e)|]$. Positive (negative) λ_e indicates chemical explosive mixtures (non-reactive or burned mixtures). At 1.207 ms in Fig. 7(a), the entire induction zone is chemically explosive, with high value of λ_{CEM} . Most of it is controlled by the chain-branching reactions with radical H having the highest EI, featuring a chemical runaway process. Thermal runaway is only observed ahead of the RF. However, near

the AS location, the importance of the gas temperature becomes greater, although it is still lower than some radical EIs, such as OH and O. At 1.2076 ms, temperature EI becomes increasingly important near the AS, indicating the developing thermal runaway area. At 1.2078 ms, the burned state is presented behind the two auto-igniting fronts, i.e., AFL and AFR, as shown in the temperature profile with $\lambda_{CEM} < 0$ in Fig. 7. Accordingly, the induction zone is divided into two un-connected chemically explosive areas, i.e., behind SF and ahead of the RF (see warm color of the gas temperature curve in Fig. 7c). The downstream one gradually shrinks as the fuel is consumed by the RF and AFL. At 1.208 ms, only the chemical explosive area between the AF and SF is observed, which is the new induction zone between the SF and new RF.

The flow field structure of pulsating detonation in water sprays is analyzed in Fig. 8, through the spatial profiles of gas temperature, velocity, shock-frame Mach number, and droplet diameter at 1.182 ms. The shock-frame subsonic zone ends at the sonic point (SP), and the gas–liquid two-phase zone ends at about $x = 1.635$ m (marked at CS). It can be observed that due to lead shock compression, the gas temperature experiences the first increase at $x = 1.769$ m, followed by a thermally neutral zone behind SF. Then chemical reaction starts at RF and the gas temperature is increased to more than 2000 K. The water droplets are heated to saturation temperature within a finite distance (about 0.006 m) behind the

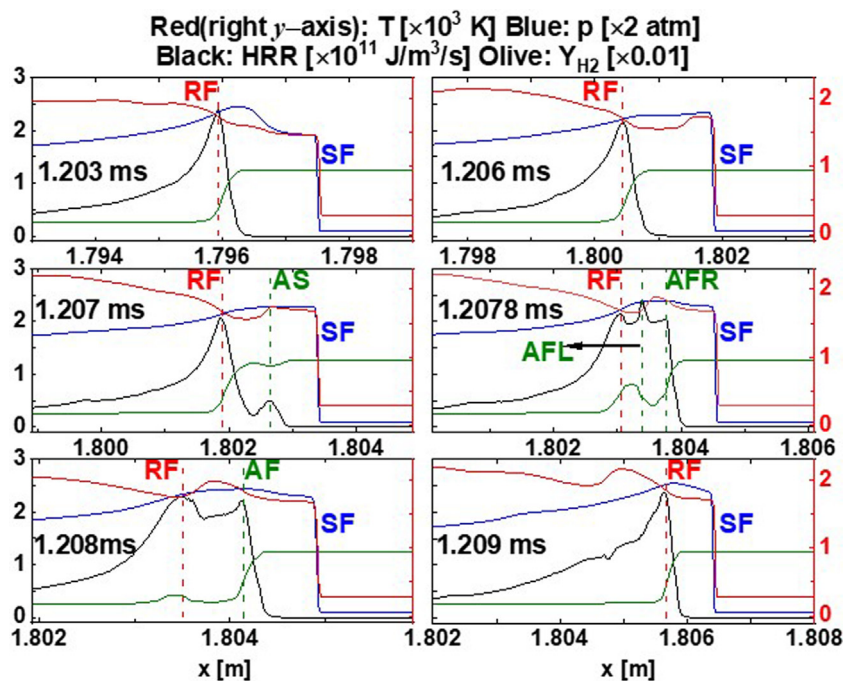


Fig. 6. Profiles of pressure, temperature, heat release rate, and H₂ mass fraction within one pulsating cycle. Red and olive dashed lines: RF and AS/AF (Autoignition Spot/Front). $d_d^0 = 5 \mu\text{m}$ and $z = 0.07$.

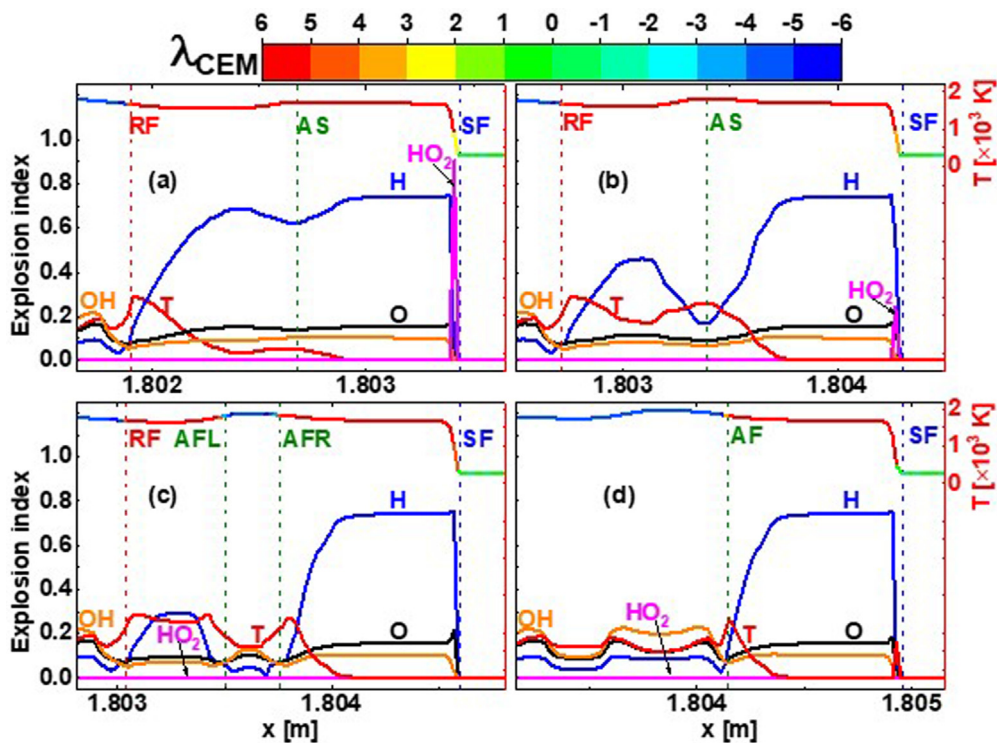


Fig. 7. Evolutions of explosion indices for species and temperature between the RF and SF at four instants: (a) 1.207, (b) 1.2076, (c) 1.2078, and (d) 1.208 ms. Gas temperature curves are colored by λ_{CEM} . $d_d^0 = 5 \mu\text{m}$ and $z = 0.07$.

SF (marked as STP). The temperature equilibrium between the gas phase and water droplets cannot be achieved; instead, large temperature difference exists and hence strong convective heat transfer proceeds in the detonated area. Moreover, the static droplets respond quickly to the high-speed flows because of short droplet momentum relaxation time, and their velocity increases behind the leading SF. Velocity quasi-equilibrium is reached ($\sim 600 \text{ m/s}$) at

about $x = 1.745 \text{ m}$ (marked as VqEP in Fig. 8). Further downstream, relatively small slip velocity always exists, which is caused by the tempo-spatial evolutions of the gas velocities behind the detonation wave and finite droplet momentum relaxation time.

The characteristic locations in spray detonations at 1.182 ms, including SF, RF, sonic point, and two-phase contact surface, are presented collectively at the top of Fig. 8. How these locations evolve

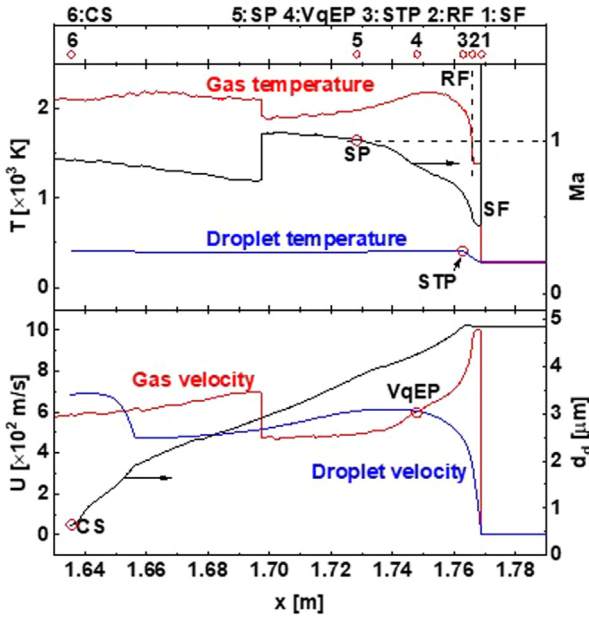


Fig. 8. Distribution of temperature, shock-frame Mach number, velocity, and droplet diameter from the case of $d_d^0 = 5 \mu\text{m}$ and $z = 0.07$ at 1.182 ms. SP: sonic point; STP: saturation temperature point; VqEP: velocity quasi-equilibrium point.

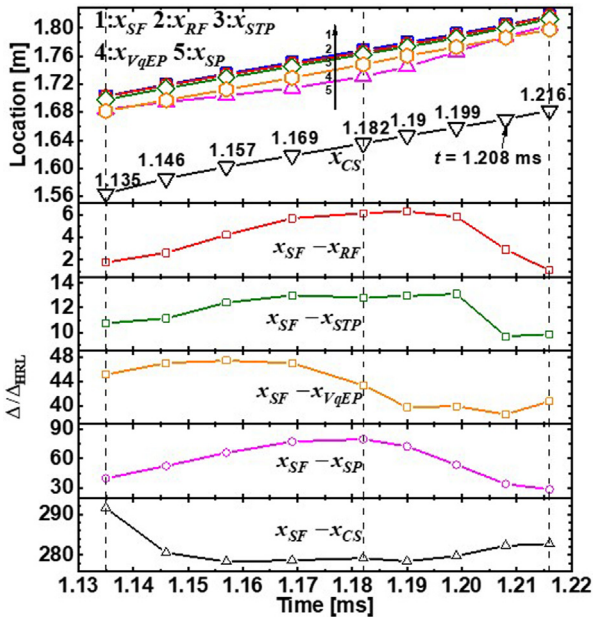


Fig. 9. Spatial evolutions of SF, RF, shock-frame sonic point, two-phase contact surface, and their distances within one pulsating cycle. $d_d^0 = 5 \mu\text{m}$ and $z = 0.07$.

in a pulsation detonation is shown in Fig. 9. Before (after) the middle dashed line, which corresponds to 1.182 ms, is the first (second) stage of the cycle. It is found that their relative positions are generally unchanged within a single pulsating period, but their distances have pronounced variations. Specifically, the induction zone length, i.e., $\Delta_x = x_{SF} - x_{RF}$, first increases and then decreases, varying between $2.0\Delta_{HRL}$ and $6.0\Delta_{HRL}$, which is already shown in Fig. 4. The similar trend is also observed in the distance of droplet saturation temperature point ($x_{SF} - x_{STP}$) relative to the shock front. This is reasonable because the gas temperature behind the SF is reduced (increased) as RF gradually decouples from (couples with) the SF in the first (second) stage.

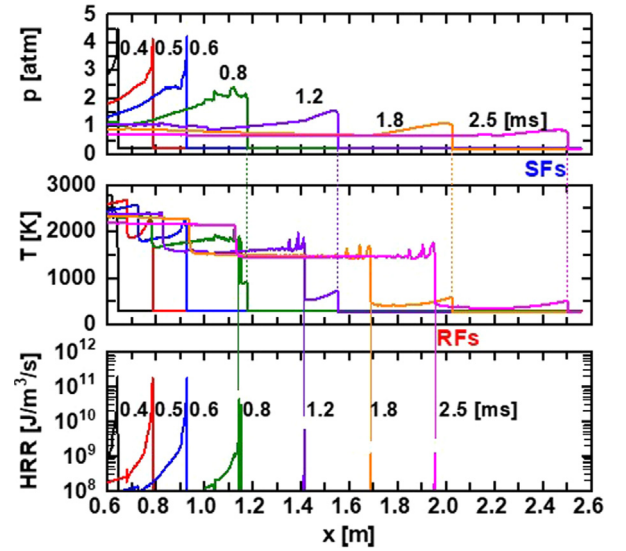


Fig. 10. Spatial evolution of pressure, gas temperature, and heat release rate. Dashed lines: SF or RF. $d_d^0 = 5 \mu\text{m}$ and $z = 0.09$. Time instants are annotated in Fig. 3.

However, the velocity quasi-equilibrium point behaves differently, with obvious delay relative to the induction zone length variation. The maximum and minimum values of $x_{SF} - x_{VqEP}$ occur inside the first and second stages, respectively. This is associated with the longer velocity response time of the water droplets. Besides, the length ($x_{SF} - x_{SP}$) of the shock-frame subsonic zone also follows the evolution trend of the induction zone length, but with larger length scales ($40\text{--}80\Delta_{HRL}$). All the above characteristic locations are in the droplet-laden area. The droplet heating / evaporation zone length in the shocked gas, $x_{SF} - x_{CS}$, also changes (between 275 and $295\Delta_{HRL}$) in the pulsation cycle. It decreases when the pulsation cycle starts, and levels off for most of the period, followed by a slow increase at the end of the pulsation cycle. The increase around the end (or the beginning) of the cycle is caused by the accelerating leading shock front and therefore more water droplets are dispersed behind the SF.

4.3. Detonation extinction

To explore the unsteady physics behind detonation failure in the second and third modes, two cases with mass loadings $z = 0.09$ and 0.25 (lines #5 and #7 in Fig. 4) are selected for discussion. Figures 10 and 11. present their time sequence of pressure, temperature, and heat release rate when the detonation wave enters the water cloud. In Fig. 10, the detonation wave travels before 0.6 ms, and after that detonation extinction is observed. Specifically, the RF and SF are decoupled, characterized by their increased distance Δ_x . For instance, from 1.2 to 2.5 ms, Δ_x increases from 0.138 to 0.548 m. Ultimately, the RF trails behind the leading SF as a premixed flame in the shocked $\text{H}_2/\text{O}_2/\text{Ar}$ mixture. The detonation extinction is also accompanied by quickly reduced peak of pressure, temperature, and heat release rate in Fig. 10. Likewise, the unsteady process of the third mode is visualized in Fig. 11. Different from the results in Fig. 10, detonation extinction occurs immediately when the detonation wave enters the two-phase area. Meanwhile, the reaction front is much weaker (with maximum HRR only about $10^4 \text{ J/m}^3/\text{s}$ at 3.5 ms) than that in Fig. 10. This is due to higher water mass loading, leading to more energy and momentum extraction from the gas phase by the evaporating droplets and thereby weaker chemical reactions.

Figures 12 and 13 demonstrate the distributions of chemical timescale τ in the induction zone of the above two cases, which

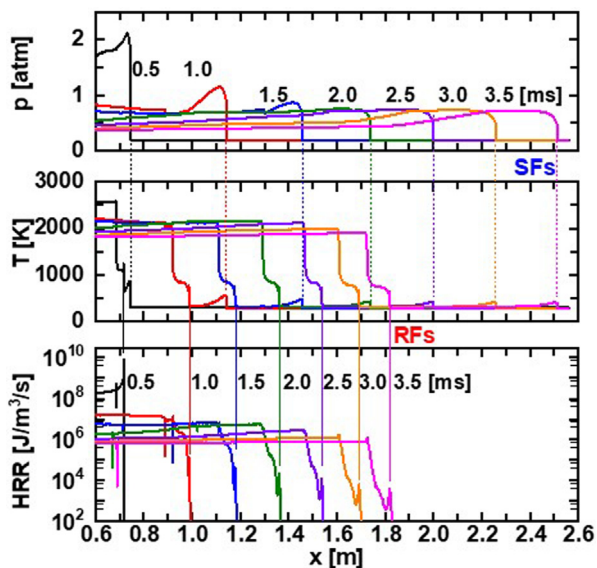


Fig. 11. Spatial evolution of pressure, gas temperature, and heat release rate. Dashed lines: SF or RF. $d_d^0 = 5 \mu\text{m}$ and $z = 0.25$. Time instants are annotated in Fig. 3.

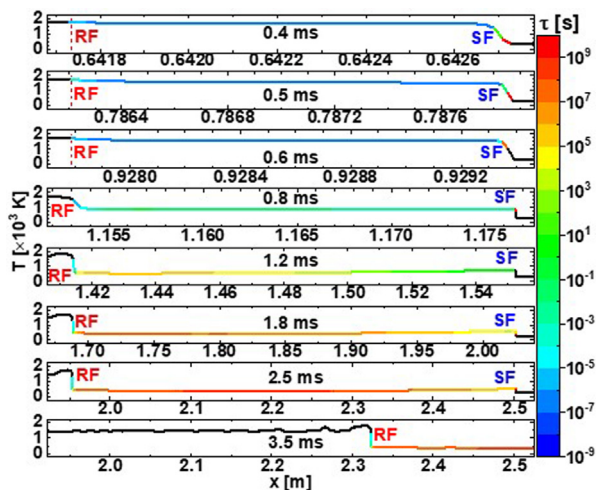


Fig. 12. Temporal evolutions of chemical timescale between the RF and SF. $d_d^0 = 5 \mu\text{m}$ and $z = 0.09$.

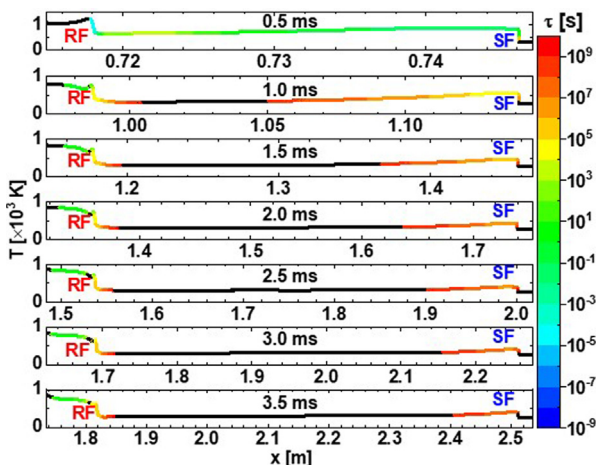


Fig. 13. Temporal evolutions of chemical timescale between the RF and SF. $d_d^0 = 5 \mu\text{m}$ and $z = 0.25$.

are colored along the gas temperature profiles. They correspond to 0.4 to 3.5 ms, and 0.5 to 3.5 ms, respectively. τ is the reciprocal of the real part of the eigenvalues, calculated from the chemical explosive mode analysis [52,54]. Only the chemically explosive mixtures (with positive real part of the eigenvalues from the chemical Jacobian matrix) are colored. At 0.4–0.6 ms for detonative combustion in Fig. 12, the chemical timescale is short, in the order of $10^{-7} - 10^{-5}$ s, indicating that the chemical reactions are still strong in the entire induction zone. However, from 0.4 to 0.6 ms, the induction zone length Δ_x increases from 1 to 1.6 mm, due to the heat absorption and/or shock attenuation by the evaporating water droplets [61–64]. Subsequently, as the RF gradually decouples from the SF after 0.8 ms, and the detonation wave is degraded into a blast wave. Meanwhile, the induction zone length is further increased to 0.6 m at 2.5 ms. Also, the chemical timescale is dramatically increased to above 10^{-3} s. The intrinsic chemical explosion propensity of the shocked mixture between RF and SF is significantly reduced. This thereby prevents the possibility of local autoignition in the shocked gas, as observed in pulsating detonations (see Figs. 6 and 7). Beyond 2.5 ms, the shocked gas is still chemical explosive but the timescale becomes high ($> 10^6$ s).

Figure 13 shows the evolutions of the chemical timescale from the third mode with higher mass loading. They are generally similar to the results in Fig. 12, but there are still striking differences. Firstly, at 0.5 ms, when the DW just enters the water cloud, the chemical timescale is much longer than the counterpart instant (e.g., 0.4 ms) in Fig. 12, indicating the stronger effects of water droplets on the chemical reactions behind the leading shock. Secondly, since 1.0 ms, the shocked mixture in the middle of the induction zone becomes not chemically explosive (see the black segments in Fig. 13) and hence the mixtures with explosion propensity become discontinuous, which is not observed in Fig. 12. Specifically, the explosive mixtures are only present immediately behind the leading SF and before the RF. These may be because the relatively high local temperature and/or radical diffusion from the RF. Meanwhile, as the distance between SF and RF increases from 1.0 ms to 3.5 ms, the extent of the explosive mixtures in the induction zone gradually shrinks, which is particularly obvious behind the SF. In addition, in the third mode, the RF is much weaker than the counterpart in Fig. 12. Therefore, even behind the RF, the mixture still has chemical explosion propensity. Compared to the second mode, the present one is featured by a more effective inhibition of hydrogen detonation by evaporating water sprays: not only do they quench the incident detonation wave, but also considerably reduce the decoupled blast wave intensity and RF reactivity. From the viewpoint of practical explosion inhibition, immediate performance of explosion inhibition by water mists is much more important, to mitigate the accidents to the largest extent and minimize the affected area. In this sense, the third mode is more desirable than the second one. Moreover, the residual reaction front from a decoupled detonation in the second mode still travel at a high speed and may lead to additional hazards, such as possible structural destruction by the blast wave [65] and deflagration-to-detonation transition for new explosion accidents [66]. Critical mass loadings to achieve the third mode and whether the effectiveness would be continuously enhanced through gradually increasing the sprayed water loading will be further discussed in Section 4.4.

Figure 14 depicts the spatial profiles of temperature, velocity, shock-frame Mach number, and droplet size in the foregoing detonation extinction cases. They respectively correspond to the instants of 1.2 and 2.5 ms. Through them, the hydrodynamic structure of spray detonations can be identified, similar to Fig. 10. They are projected to the x-axis and shown at the top of the figures. It is observed from Fig. 14(a) that the relative positions of the SF, RF, STP, VqEP, and two-phase CS have changed, compared to the deto-

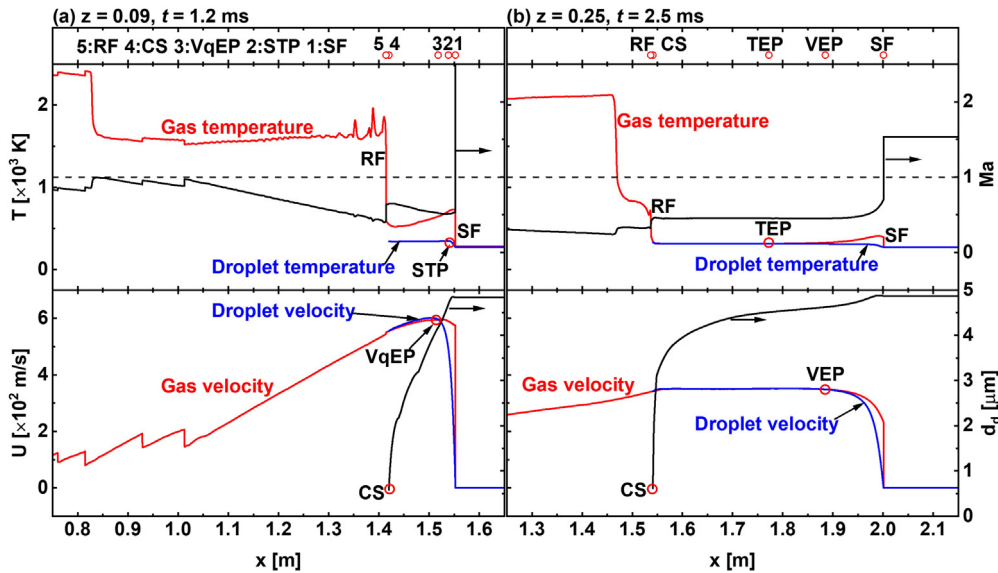


Fig. 14. Distributions of temperature, velocity, shock-frame Mach number and droplet diameter: (a) $z = 0.09$ and (b) $z = 0.25$. $d_d^0 = 5 \mu\text{m}$. CS: two-phase contact surface; STP: saturation temperature point; TEP: temperature equilibrium point; VEP: velocity equilibrium point; VqEP: velocity quasi-equilibrium point.

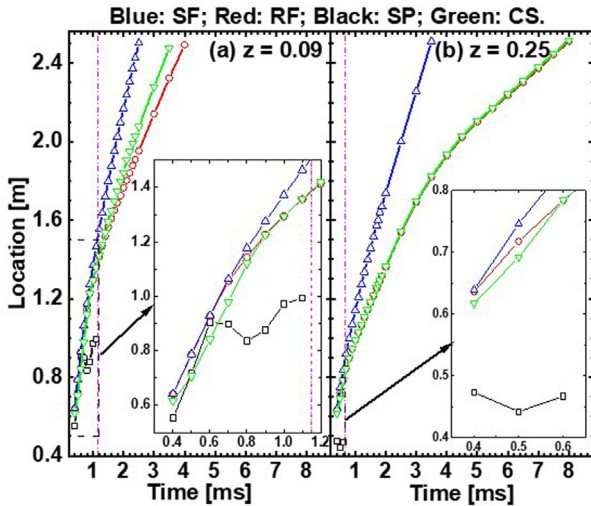


Fig. 15. Time evolutions of characteristic locations in the course of detonation extinction: (a) $z = 0.09$ and (b) $z = 0.25$. $d_d^0 = 5 \mu\text{m}$. Dash-dotted lines demarcate homogeneous and heterogeneous RF.

nation results in Fig. 8. Specifically, the RF is well behind all other locations, and the shocked flow velocity relative to the leading SF is subsonic (hence absent SP). From Fig. 14(b), one can see that these locations have evolved into the following order, i.e., SF, velocity equilibrium point (VEP), temperature equilibrium point (TEP), CS and RF. Different from the situations in Figs. 14(a) and 8, the kinematic and thermal equilibria between the shocked gas and water droplets are achieved. This is because the lengthened distance between SF and RF and therefore the momentum and thermal relaxation timescales can be reached.

The time evolutions of spray detonation flow structure in the course of detonation extinction by water sprays is shown in Fig. 15. When the water loading is 0.09, it is observed from Fig. 15(a) that the distance between the SF and RF gradually increases. Before 1.2 ms (dashed-dotted line), the two-phase contact surface is well behind the SF and RF (see the inset of the Fig. 15a). Therefore, the mixture around the RF is heterogeneous (gas and droplets). After that, due to increased induction length, the droplets complete

the evaporation well ahead of the reaction front (i.e., $x_{CS} > x_{RF}$), as seen from Fig. 15(a). This indicates that after detonation extinction, the mixture before the RF is homogeneous (gas only) and the RF evolves as a gaseous premixed flame in shocked $\text{H}_2/\text{O}_2/\text{Ar}/\text{H}_2\text{O}$ mixture. Water vapor addition as a diluent and latent heat absorption jointly reduce the chemical reactivity. This can also be observed when the water mass loading is 0.25 in Fig. 15(b). However, because of high water loading, the distance between the two-phase contact surface and RF is smaller in Fig. 15(b). The homogeneous and heterogeneous flame propagation in water sprays is found to have different dynamic behaviours, based on a recent theoretical analysis for laminar flames by Zhuang and Zhang [67,68]. Further studies are merited, from both fundamental and practical hazard prevention perspectives, to unveil the interactions between the residual RF and dispersed droplets after detonation extinction. In addition, from Fig. 15(b), the RF and CS have similar propagation speeds, e.g., about 145 m/s after 4 ms. For both cases, after detonation extinction, the shock-frame sonic points (see the squares in Fig. 15) generally move downstream after the detonation encroaches the water clouds. Beyond about 1.1 ms and 0.7 ms respectively in two cases (see their insets), the shocked gas become subsonic in the shock frame.

4.4. Diagram of detonation propagation and extinction in water sprays

The unsteady detonation phenomena, including detonation pulsation propagation and extinction, are further generalized through considering different initial droplet diameters d_d^0 and mass loadings z . The results are summarized in the diagram of droplet size and mass loading in Fig. 16. The dashed line is the critical condition for extinction (including the second and third modes) of the incident $\text{H}_2/\text{O}_2/\text{Ar}$ detonations in the water sprays. Apparently, when the initial droplet size is reduced, the critical mass loading for detonation extinction, z_{ext} , decreases considerably. For instance, $z_{ext} = 0.08$ for $5 \mu\text{m}$, whilst it is increased to 0.375 for $15 \mu\text{m}$. This is reasonable because smaller droplets have fast evaporation rate and larger specific droplet surface area and hence are more effective in inhibiting the detonation wave. Meanwhile, when the water loading is sufficiently large, e.g., $z > 0.2$, detonation extinction always occurs (except the case of $z = 0.25$ and $d_d^0 = 15 \mu\text{m}$), for all the con-

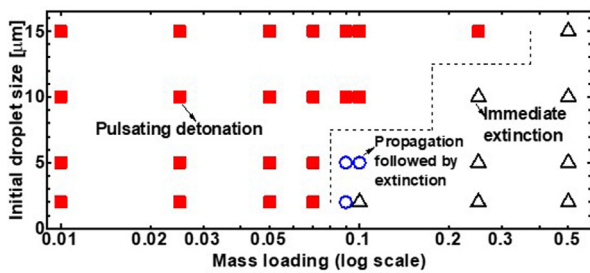


Fig. 16. Diagram of detonation propagation and extinction in fine water sprays. Squares: detonation propagation; triangles: immediate extinction; circles: propagation followed by extinction.

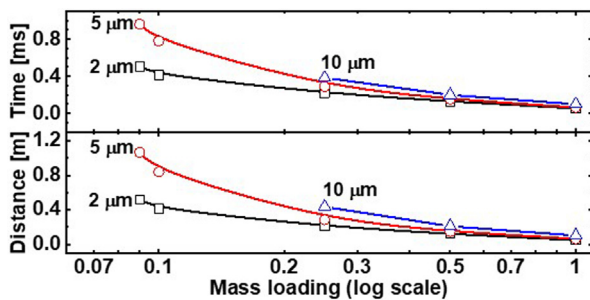


Fig. 17. Extinction time and distance as functions of water mass loading and initial droplet size.

sidered droplet size. Moreover, when $z < 0.07$, the detonation wave can always successfully cross the water cloud in a galloping fashion, regardless of droplet size. However, when $z = 0.09$ and 0.1 , the droplet diameter effect becomes pronounced: for these two loadings, finer droplets with $d_d^0 \leq 5 \mu\text{m}$ are necessary to quench the incident detonations.

To measure the effectiveness of various water droplets in detonation inhibition, extinction time and distance in the detonation failure cases are shown in Fig. 17. In our study, they are respectively defined as the duration and distance when the detonation travels in the water sprays and the leading shock speed is reduced to half of the C-J velocity of the dry mixture D_{CJ} . For a fixed water spray diameter, both extinction time and distance decrease monotonically with mass loading. Meanwhile, when the mass loading is fixed, the extinction time / distance monotonically increases with the droplet diameter. Interestingly, when the mass loading is increased beyond 0.5, the extinction time / distance corresponding to three diameters are very close. Therefore, continuously increasing the water mass loading does not proportionally increase the effectiveness of fine water sprays for detonation extinction; instead, the extinction time and distance would approach the asymptotic values, i.e., 0.1 m and 0.07 ms. This is essentially limited by the finite timescale of two-phase coupling between gas and droplet phases, such as heat transfer and droplet evaporation. For practical implementations of explosion prevention, this result implies that: (1) when the water loading is sufficiently high, the effectiveness in detonation inhibition has weak dependence on sprayed droplet sizes; and (2) these asymptotic values can be important reference for designing water curtain dimensions.

Pulsating detonations are seen in all the stable cases in Fig. 16, and their average leading shock speed is shown in Fig. 18. It is observed that the detonation speeds in two-phase medium are consistently lower than that in water-free case ($D/D_{CJ} < 1$). One can see from Fig. 18(a) that for a fixed water mass loading, the shock speed is higher when the droplet size is higher. This is reasonable because the larger diameter corresponds to a smaller specific surface area, and therefore slower two-phase exchange about mass,

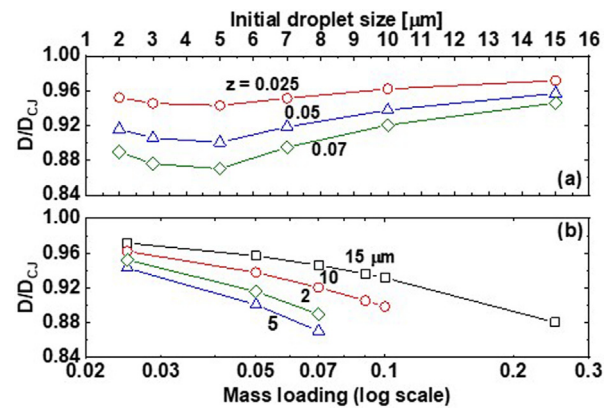


Fig. 18. Change of leading shock propagation speed with (a) droplet diameter and (b) mass loading. D_{CJ} : C-J speed of water-free $\text{H}_2/\text{O}_2/\text{Ar}$ mixture.

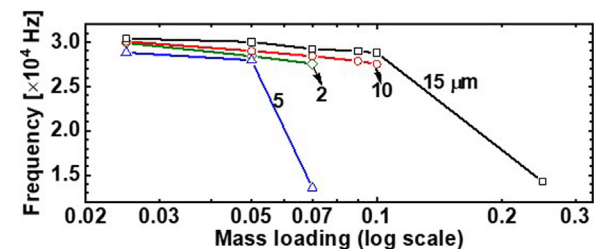


Fig. 19. Change of pulsation frequency with mass loading and droplet size.

momentum, and energy. However, an opposite tendency is seen for fine droplets and a minimum speed exists around $d_d^0 = 5 \mu\text{m}$. This is because when the droplet diameter is smaller than $5 \mu\text{m}$, such as $d_d^0 = 2 \mu\text{m}$, the magnitudes of interphase transfer (e.g., energy and momentum absorption from the gas) are generally lower than those of the $5 \mu\text{m}$ droplets. This results in higher speeds with the finer droplets compared to that of $5 \mu\text{m}$. These can be well confirmed from the timeseries of the integrated interphase transfer in Section C of Supplementary Document. Moreover, one can see from Fig. 18(b), the average speeds monotonically decrease with mass loading for a fixed droplet size, because transferred heat and momentum become greater.

In addition, the effects of droplet diameter and mass loading on pulsation frequency are shown in Fig. 19. Generally, the frequency varies between 2.6×10^4 and 3.1×10^4 Hz, except the two case near the extinction critical condition. For all the droplet sizes in Fig. 19, the frequency decreases when the mass loading becomes larger. This is because the RF-SF coupling is weakened by stronger interphase exchange, indicating that the RF and SF need longer time to complete one pulsation cycle. For the same mass loading (such as 0.05), the pulsating frequency shows non-monotonic evolution with initial droplet size. Like the results of shock speed in Fig. 18, the case with $d_d^0 = 5 \mu\text{m}$ has the smallest frequency, which is related to higher energy and momentum extraction from the gas phase.

5. Conclusions

Pulsating detonation in gas-droplet two-phase mixtures is studied by Eulerian-Lagrangian approach with two-way coupling. Detailed chemical mechanism is used for stoichiometric hydrogen/oxygen/argon detonation, and ultrafine mono-sized water droplets are considered, covering a range of droplet size and mass loading.

Three detonation propagation modes are observed: (1) pulsating propagation, (2) extinction after a finite propagation, and (3) immediate extinction. For pulsating detonation, the propagation speeds of RF and SF and their distance is found to have periodic changes. Within one cycle, multiple pressure waves are generated from the RF, which overtake and intensify the leading shock. An autoigniting spot arises in the shocked gas, which is confirmed from the eigenvalue evolutions of the chemical Jacobian matrix in chemical explosive mode analysis. The evolutions of the characteristic locations in the flow structure of spray detonations, including SF, RF, shock-frame sonic point, and two-phase contact surface are also analyzed. The results show that their relative positions remain unchanged within one pulsating cycle, but their distances are shown to have periodic variations.

The unsteady behaviors of detonation extinction are also studied. The results reveal that the decoupling of RF and SF is accompanied by considerably increased chemical timescale of the shocked mixture, and part of the mixture behind SF is even chemically non-explosive due to relatively low temperature. The relative positions of the characteristic locations in spray detonations also change significantly. The reaction front trails behind all other characteristic fronts, and the post-shock flow is subsonic in the shock frame. The results also demonstrate that gas-only mixtures exist before the RF due to the complete evaporation of the droplets, and hence the RF behaves like a gaseous premixed flame in $H_2/O_2/Ar/H_2O$ mixture.

A map of detonation pulsating propagation and failure considering various water mass loadings and initial droplet sizes are predicted through detailed 1D simulations. It shows that the critical mass loading for detonation extinction decreases when the droplet size becomes smaller. Moreover, the detonation extinction distance and time decrease with increased water loading and reduced droplet size. Asymptotic values of extinction time and distance exist (0.1 m and 0.07 ms, respectively) when the water loading is beyond 0.5. Moreover, the frequency and average speed of pulsating detonation is shown to have non-monotonic dependence on the droplet size but monotonically decreases with water mass loading.

Declaration of Competing Interest

The authors declare that they have no known competing financial interests or personal relationships that could have appeared to influence the work reported in this paper.

Acknowledgements

This work used the computational resources of ASPIRE 1 Cluster in The National Supercomputing centre, Singapore (<https://www.nsc.sg>). YX is supported by the NUS Research Scholarship. This research is supported by the National Research Foundation, Prime Minister's Office, Singapore under its Campus for Research Excellence and Technological Enterprise (CREATE) program (R-265-000-A57-592). Professor Zhuyin Ren and Dr Wantong Wu at Tsinghua University are thanked for sharing the CEMA subroutines. Professor Michael P. Burke from Columbia University is also appreciated for helpful discussions about the chemical mechanism.

Declarations of Competing Interest

None.

Supplementary materials

Supplementary material associated with this article can be found, in the online version, at [doi:10.1016/j.combustflame.2022.112086](https://doi.org/10.1016/j.combustflame.2022.112086).

References

- [1] F. Olmos, V.I. Manousiouthakis, Hydrogen car fill-up process modeling and simulation, *Int. J. Hydrogen Energy* 38 (2013) 3401–3418.
- [2] C. Catlin, Passive explosion suppression by blast-induced atomisation from water containers, *J. Hazard. Mater.* 94 (2002) 103–132.
- [3] G.O. Thomas, On the conditions required for explosion mitigation by water sprays, *Process Saf. Environ. Prot.* 78 (2000) 339–354.
- [4] G. Grant, J. Brenton, D. Drysdale, Fire suppression by water sprays, *Prog. Energy Combust. Sci.* 26 (2000) 79–130.
- [5] G.O. Thomas, M.J. Edwards, D.H. Edwards, Studies of detonation quenching by water sprays, *Combust. Sci. Technol.* 71 (1990) 233–245.
- [6] U. Niedzielska, L.J. Kapusta, B. Savard, A. Teodorczyk, Influence of water droplets on propagating detonations, *J. Loss Prev. Process Ind.* 50 (2017) 229–236.
- [7] G. Jarsalé, F. Virot, A. Chinnayya, Ethylene–air detonation in water spray, *Shock Waves* 26 (2016) 561–572.
- [8] Y. Song, Q. Zhang, Quantitative research on gas explosion inhibition by water mist, *J. Hazard. Mater.* 363 (2019) 16–25.
- [9] H. Watanabe, A. Matsuo, A. Chinnayya, K. Matsuoka, A. Kawasaki, J. Kasahara, Numerical analysis of the mean structure of gaseous detonation with dilute water spray, *J. Fluid Mech.* 887 (2020) A4–1–40.
- [10] H. Watanabe, A. Matsuo, A. Chinnayya, K. Matsuoka, A. Kawasaki, J. Kasahara, Numerical analysis on behavior of dilute water droplets in detonation, *Proc. Combust. Inst.* (2020) 1–8 000.
- [11] J.H.S. Lee, *The Detonation Phenomenon*, Cambridge University Press, 2008.
- [12] J.B. McVey, T.Y. Toong, Mechanism of instabilities of exothermic hypersonic blunt-body flows, *Combust. Sci. Technol.* 3 (1971) 63–76.
- [13] L.R. ALPERT, T.Y. Toong, Periodicity in exothermic hypersonic flows about blunt projectiles, *Acta Astronaut.* 17 (1972) 539–560.
- [14] Y. Daimon, A. Matsuo, Detailed features of one-dimensional detonations, *Phys. Fluids* 15 (2003) 112–122.
- [15] S. Yungster, K. Radhakrishnan, Pulsating one-dimensional detonations in hydrogen–air mixtures, *Combust. Theory Model.* 8 (2004) 745–770.
- [16] C. Leung, M.I. Radulescu, G.J. Sharpe, Characteristics analysis of the one-dimensional pulsating dynamics of chain-branching detonations, *Phys. Fluids* 22 (2010) 126101.
- [17] S. Yungster, K. Radhakrishnan, Structure and stability of one-dimensional detonations in ethylene–air mixtures, *Shock Waves* 14 (2005) 61–72.
- [18] M. Short, A.K. Kapila, J.J. Quirk, The chemical-gas dynamic mechanisms of pulsating detonation wave instability, *Philos. Trans. R. Soc. London. Ser. A Math. Phys. Eng. Sci.* 357 (1999) 3621–3637.
- [19] M.A. Sussman, *Numerical Simulation of Shock-Induced Combustion*, Doctoral dissertation, Stanford University, 1995.
- [20] H.D. Ng, M.I. Radulescu, A.J. Higgins, N. Nikiforakis, J.H.S. Lee, Numerical investigation of the instability for one-dimensional Chapman-Jouguet detonations with chain-branching kinetics, *Combust. Theory Model.* 9 (2005) 385–401.
- [21] H.D. Ng, A.J. Higgins, C.B. Kiyanda, M.I. Radulescu, J.H.S. Lee, K.R. Bates, N. Nikiforakis, Nonlinear dynamics and chaos analysis of one-dimensional pulsating detonations, *Combust. Theory Model.* 9 (2005) 159–170.
- [22] W. Han, C. Wang, C.K. Law, Pulsation in one-dimensional H_2 - O_2 detonation with detailed reaction mechanism, *Combust. Flame* 200 (2019) 242–261.
- [23] W. Han, W. Ma, C. Qian, J. Wen, C. Wang, Bifurcation of pulsation instability in one-dimensional H_2 - O_2 detonation with detailed reaction mechanism, *Phys. Rev. Fluids* 4 (2019) 1–15.
- [24] M. Kim, X. Mi, C.B. Kiyanda, H.D. Ng, Nonlinear dynamics and chaos regularization of one-dimensional pulsating detonations with small sinusoidal density perturbations, *Proc. Combust. Inst.* (2020) 1–8 000.
- [25] M. Zhao, Z. Ren, H. Zhang, Pulsating detonative combustion in n-heptane/air mixtures under off-stoichiometric conditions, *Combust. Flame* 226 (2021) 285–301.
- [26] Z. Huang, M. Zhao, Y. Xu, G. Li, H. Zhang, Eulerian-Lagrangian modelling of detonative combustion in two-phase gas-droplet mixtures with OpenFOAM: validations and verifications, *Fuel* 286 (2021) 119402.
- [27] M. Zhao, H. Zhang, Large eddy simulation of non-reacting flow and mixing fields in a rotating detonation engine, *Fuel* 280 (2020) 118534.
- [28] H.G. Weller, G. Tabor, H. Jasak, C. Fureby, A tensorial approach to computational continuum mechanics using object-oriented techniques, *Comput. Phys.* 12 (1998) 620.
- [29] G.B. Macpherson, N. Nordin, H.G. Weller, Particle tracking in unstructured, arbitrary polyhedral meshes for use in CFD and molecular dynamics, *Commun. Numer. Methods Eng.* 25 (2009) 263–273.
- [30] C. Crowe, J. Schwarzkopf, M. Sommerfeld, Y. Tsuji, *Multiphase Flows with Droplets and Particles*, 2nd ed., CRC Press, 2011.
- [31] W.E. Ranz, W.R. Marshall, Evaporation from drops, part I, *Chem. Eng. Prog.* 48 (1952) 141–146.
- [32] E.N. Fuller, P.D. Schettler, J.C. Giddings, A new method for prediction of binary gas - phase diffusion coefficients, *Ind. Eng. Chem.* 58 (1966) 18–27.

- [33] A.B. Liu, D. Mather, R.D. Reitz, Modeling the effects of drop drag and breakup on fuel sprays, SAE Tech. Pap. (1993) 1.
- [34] C.T. Crowe, M.P. Sharma, D.E. Stock, The particle-source-in cell (PSI-CELL) model for gas-droplet flows, *J. Fluids Eng.* 99 (1977) 325–332.
- [35] Y. Xu, M. Zhao, H. Zhang, Extinction of incident hydrogen/air detonation in fine water sprays, *Phys. Fluids* 33 (2021) 116109.
- [36] A. Kurganov, S. Noelle, G. Petrova, Semidiscrete central-upwind schemes for hyperbolic conservation laws and Hamilton–Jacobi equations, *SIAM J. Sci. Comput.* 23 (2001) 707–740.
- [37] C.J. Greenshields, H.G. Weller, L. Gasparini, J.M. Reese, Implementation of semi-discrete, non-staggered central schemes in a collocated, polyhedral, finite volume framework, for high-speed viscous flows, *Int. J. Numer. Methods Fluids* 63 (2010) 1–21.
- [38] M.P. Burke, M. Chaos, Y. Ju, F.L. Dryer, S.J. Klippenstein, Comprehensive H₂/O₂ kinetic model for high-pressure combustion, *Int. J. Chem. Kinet.* 44 (2012) 444–474.
- [39] M. Zhao, J.M. Li, C.J. Teo, B.C. Khoo, H. Zhang, Effects of variable total pressures on instability and extinction of rotating detonation combustion, *Flow, Turbul. Combust.* 104 (2020) 261–290.
- [40] M. Zhao, H. Zhang, Origin and chaotic propagation of multiple rotating detonation waves in hydrogen/air mixtures, *Fuel* 275 (2020) 117986.
- [41] M. Zhao, H. Zhang, Modelling rotating detonative combustion fueled by partially pre-vaporized n-heptane sprays, *Accept. by 38th Int. Symp. Combust. under Rev. by Proc. Combust. Inst.* (2021).
- [42] Q. Meng, M. Zhao, H. Zheng, H. Zhang, Eulerian–Lagrangian modelling of rotating detonative combustion in partially pre-vaporized n-heptane sprays with hydrogen addition, *Fuel* (2020) 119808.
- [43] M. Zhao, Z.X. Chen, H. Zhang, N. Swaminathan, Large Eddy simulation of a supersonic lifted hydrogen flame with perfectly stirred reactor model, *Combust. Flame* 230 (2021) 0–51.
- [44] R. Zhu, M. Zhao, H. Zhang, Numerical simulation of flame acceleration and deflagration-to-detonation transition in ammonia-hydrogen-oxygen mixtures, *Int. J. Hydrogen Energy* 46 (2021) 1273–1287.
- [45] K. Mazaheri, Y. Mahmoudi, M.I. Radulescu, Diffusion and hydrodynamic instabilities in gaseous detonations, *Combust. Flame* 159 (2012) 2138–2154.
- [46] K. Luo, O. Desjardins, H. Pitsch, DNS of droplet evaporation and combustion in a swirling combustor, *Cent. Turbul. Res. Annu. Res. Briefs* (2008) 253–265.
- [47] S.S. Sazhin, P.A. Krutitskii, S.B. Martynov, D. Mason, M.R. Heikal, E.M. Sazhina, Transient heating of a semitransparent spherical body, *Int. J. Therm. Sci.* 46 (2007) 444–457.
- [48] M. Sontheimer, A. Kronenburg, O.T. Stein, Grid dependence of evaporation rates in Euler–Lagrange simulations of dilute sprays, *Combust. Flame* 232 (2021) 111515.
- [49] X.J. Gu, D.R. Emerson, D. Bradley, Modes of reaction front propagation from hot spots, *Combust. Flame* 133 (2003) 63–74.
- [50] K.C. Tang-Yuk, X.C. Mi, J.H.S. Lee, H.D. Ng, R. Deiterding, Transmission of a detonation wave across an inert layer, *Combust. Flame* 236 (2022) 111769.
- [51] Y. Daimon, A. Matsuo, Unsteady features on one-dimensional hydrogen-air detonations, *Phys. Fluids* 19 (2007) 116101.
- [52] T.F. Lu, C.S. Yoo, J.H. Chen, C.K. Law, Three-dimensional direct numerical simulation of a turbulent lifted hydrogen jet flame in heated coflow: a chemical explosive mode analysis, *J. Fluid Mech.* 652 (2010) 45–64.
- [53] D.A. Goussis, H.G. Im, H.N. Najm, S. Paolucci, M. Valorani, The origin of CEMA and its relation to CSP, *Combust. Flame* 227 (2021) 396–401.
- [54] S.H. Lam, D.A. Coussis, Understanding complex chemical kinetics with computational singular perturbation, *Symp. Combust.* 22 (1989) 931–941.
- [55] W. Wu, Y. Piao, Q. Xie, Z. Ren, Flame diagnostics with a conservative representation of chemical explosive mode analysis, *AIAA J.* 57 (2019) 1355–1363.
- [56] S.H. Lam, Using CSP to understand complex chemical kinetics, *Combust. Sci. Technol.* 89 (1993) 375–404.
- [57] W. Xie, W. Wu, Z. Ren, H. Liu, M. Ihme, Effects of evaporation on chemical reactions in counterflow spray flames, *Phys. Fluids* 33 (2021) 065115.
- [58] W. Wu, Y. Piao, Q. Xie, Z. Ren, Flame diagnostics with a conservative representation of chemical explosive mode analysis, *AIAA J.* 57 (2019) 1355–1363.
- [59] Z. Luo, C.S. Yoo, E.S. Richardson, J.H. Chen, C.K. Law, T. Lu, Chemical explosive mode analysis for a turbulent lifted ethylene jet flame in highly-heated coflow, *Combust. Flame* 159 (2012) 265–274.
- [60] R. Shan, C.S. Yoo, J.H. Chen, T. Lu, Computational diagnostics for n-heptane flames with chemical explosive mode analysis, *Combust. Flame* 159 (2012) 3119–3127.
- [61] Z. Huang, H. Zhang, On the interactions between a propagating shock wave and evaporating water droplets, *Phys. Fluids* 32 (2020) 123315.
- [62] J. Kersey, E. Loth, D. Lankford, Effects of evaporating droplets on shock waves, *AIAA J.* 48 (2010) 1975–1986.
- [63] U. Niedzielska, L.J. Kapusta, B. Savard, A. Teodorczyk, Influence of water droplets on propagating detonations, *J. Loss Prev. Process Ind.* 50 (2017) 229–236.
- [64] G. Jourdan, L. Biamino, C. Mariani, C. Blanchot, E. Daniel, J. Massoni, L. Houas, R. Tosello, D. Praguine, Attenuation of a shock wave passing through a cloud of water droplets, *Shock Waves* 20 (2010) 285–296.
- [65] K. Kailasanath, P.A. Tatem, F.W. Williams, J. Mawhinney, Blast mitigation using water – a status report, *Tech. Rep.* (2002).
- [66] E.S. Oran, V.N. Gamezo, Origins of the deflagration-to-detonation transition in gas-phase combustion, *Combust. Flame* 148 (2007) 4–47.
- [67] Y. Zhuang, H. Zhang, Effects of water droplet evaporation on initiation, propagation and extinction of premixed spherical flames, *Int. J. Multiph. Flow* 117 (2019) 114–129.
- [68] Y. Zhuang, H. Zhang, On flame bifurcation and multiplicity in consistently propagating spherical flame and droplet evaporation fronts, *Int. J. Multiph. Flow* 125 (2020) 103220.